Effects of alloy heat treatment on oxidation kinetics and scale morphology for Crofer 22 APU

Neal J. Magdefrau [a,*], Lei Chen [a], Ellen Y. Sun [a], Mark Aindow [b]

[a] United Technologies Research Center, East Hartford, CT 06108, USA
[b] Department of Materials Science and Engineering, Institute of Materials Science, University of Connecticut, Storrs, CT 06269, USA

HIGHLIGHTS

- Heat treatment gives a reduction in parabolic oxidation constant of up to 3.5×.
- Scales have a continuous Cr_2O_3 layer and a discontinuous $MnCr_2O_4$ spinel layer.
- The proportion and grain size of the spinel increased with alloy heat treatment.
- Nucleation of the Cr_2O_3 and $MnCr_2O_4$ influences the final scale microstructures.
- Larger alloy grain sizes lead to improved oxidation resistance.

ARTICLE INFO

ABSTRACT

The effect of alloy heat treatment on the oxidation kinetics and oxide scale microstructure of Crofer 22 APU has been studied. Parabolic oxidation rate constants were measured for the as-received alloy and after pre-oxidation heat treatment in argon at 1050 °C for 1 and 4 h. The oxide scale microstructure was investigated using scanning electron microscopy, focused ion beam milling and transmission electron microscopy. It was found that the alloy forms a two-layer scale with a continuous chromia layer and a discontinuous $MnCr_2O_4$ overlayer. Two forms of internal oxides were also formed: subscale pockets of spinel and isolated TiO_x precipitates in the underlying alloy. The pre-oxidation heat treatment had a profound effect on the grain size and morphology of the Cr_2O_3 and $MnCr_2O_4$ layers in the scale. The heat-treated samples exhibit a 3.5× lower parabolic oxidation rate constant than the as-received Crofer 22 APU. This improvement in oxidation resistance is attributed to the dramatic differences in the morphology of the oxide scale that forms during the earliest stages of oxidation (<5 h). The implications of these findings for oxidation mechanisms and long-term SOFC performance are discussed.

1. Introduction

Solid Oxide Fuel Cells (SOFCs) are an attractive option for power generation due to their excellent system efficiencies and fuel flexibility. Recent improvements in electrolyte materials have decreased the operating temperatures for SOFCs to between 650 and 800 °C, which enables metallic interconnects to be used in place of the traditional ceramic interconnect materials. Ferritic stainless steels and Ni-base alloys are currently regarded as the most promising materials for these metallic interconnects due to the semiconducting properties of their native chromia (Cr_2O_3) scales. Unfortunately, such chromia scales can be oxidized further on the cathode side of SOFCs leading to the formation of volatile hexavalent chromium species that can redeposit onto the ceramic cathode causing poisoning [1–3]. Thus, SOFC interconnect alloys typically require protective coatings to suppress the formation of these volatile chromium species [4,5].

Crofer 22 APU (ThyssenKrupp AG, Germany) is a ferritic stainless steel developed specifically for SOFC interconnect applications [6]. The composition limits for the alloy are given in Table 1; the Mn is intended to promote the formation of a $(Mn,Cr)_3O_4$ spinel overlayer on top of the chromia scale and thus to obviate the need for a protective coating. Yang et al. measured an oxidation rate constant (k_g) of 8.0×10^{-14} g^2 cm^{-4} s^{-1} for Crofer 22 APU oxidized in air at 800 °C [7], and this falls within the range of rate constants reported for ferritic stainless steels in a review by Fergus [8]. Unfortunately, this oxidation rate is not sufficiently low to enable uncoated Crofer 22 APU interconnects to meet the current 40,000 h SOFC lifetime

* Corresponding author. Tel.: +1 860 610 7403; fax: +1 860 660 4512.
E-mail address: magdefnj@utrc.utc.com (N.J. Magdefrau).

Table 1
Composition specification for Crofer 22 APU. All values are in wt.%.

	Cr	Fe	C	Mn	Si	Cu	Al	S	P	Ti	La
min	20.0			0.30						0.03	0.04
max	24.0	Bal.	0.03	0.80	0.50	0.50	0.50	0.02	0.05	0.20	0.20

requirement. Life prediction models based on thermal expansion and residual stress calculations performed by Liu et al. indicated that the maximum allowable oxide scale thickness to avoid oxide spallation is around 11 μm [9]. Using the oxidation rate constant measured by Yang et al., this would imply that scale formed on Crofer 22 APU would become mechanically unstable after less than 5000 h exposure. Moreover, SOFC tests performed by Stanislowski et al. using bare Crofer showed a performance degradation rate of 21%/1000 h [2]; this rate is two orders of magnitude higher than the value that can be tolerated for long-term SOFC applications. Thus, as for all other SOFC interconnect alloys, Crofer 22 APU requires a protective coating both to retard the oxidation rate and to prevent the egress of volatile chromium species. The requirements for such coatings are rather stringent. They must be: electrically conductive, oxidation resistant, and have minimal open porosity. The most successful coatings to date have been based on manganese cobaltite ((Mn,Co)$_3$O$_4$- MCO). The MCO composition that has received most attention is Mn$_{1.5}$Co$_{1.5}$O$_4$, which exhibits electrical conductivities of >60 S cm^{-1} at 800 °C [10].

In recent work by the present authors [11] Mn$_{1.5}$Co$_{1.5}$O$_4$ coatings were applied to Crofer 22 APU samples using the slurry coating process described by Yang et al. [10]. The coated samples were oxidized at 800 °C in air for times of up to 1000 h and the microstructures of the as-deposited and the oxidized coatings were analyzed by cross-sectional transmission electron microscopy (TEM). It was shown that a complex series of spinel reaction products developed between the MCO coating and the Crofer substrate; these included (Mn, Co, Cr, Fe)$_3$O$_4$ layers between the chromia and the MCO and pockets of stoichiometric MnCr$_2$O$_4$ at the chromia/alloy interface. These reaction products could have important consequences for the degradation of MCO-coated Crofer interconnects during long-term service in SOFCs, but a full elucidation of these phenomena will require a more detailed understanding of the basic oxidation characteristics for Crofer 22 APU than is currently available in the literature.

In previous oxidation studies it has been shown that a two-layer scale forms on Crofer 22 APU. This microstructure comprises a compact Cr$_2$O$_3$ layer on the metallic substrate and an outer (Mn,Cr)$_3$O$_4$ spinel phase on top of the Cr$_2$O$_3$, as intended by the alloy designers. An XRD study of scale development on Crofer 22 APU at 800 °C by Yang et al. showed that both Cr$_2$O$_3$ and (Mn,Cr)$_3$O$_4$ formed after only 2 h of exposure in air [12]. The same two oxidation products have also been reported as being stable in dual atmosphere (moist H$_2$/air) [13] and in SO$_2$ containing atmospheres [14]. While there have been several published oxidation studies on Crofer 22 APU, to our knowledge there have been no investigations on the effects of alloy microstructure on oxidation kinetics and scale morphology.

In this paper, we describe a study of the microstructure in the oxide scale formed on Crofer 22 APU in static air at 800 °C. Crofer samples were used in both the as-received (cold-worked and recovered) condition and after pre-oxidation heat treatment to modify the grain size. It is well known that alloy grain boundaries can act as rapid diffusion paths for both anions and cations, and so the starting alloy grain size could have a profound influence on the nucleation and growth of the native oxide scale. However, it is not clear what this effect will be: in some chromia-forming steels a smaller alloy grain size leads to improved oxidation resistance (e.g.

Ref. [15]), whereas in others the opposite trend is observed (e.g. Ref. [16]). Here we show that a larger grain size leads to a dramatic reduction in the oxidation rate for Crofer 22 APU and that this is accompanied by changes in the character and morphology of the oxide scale. These observations are used to deduce the role that grain boundary diffusion plays in oxide scale development and to provide a useful baseline for comparison with the microstructures in the oxide scales of coated Crofer 22 APU samples.

2. Experimental

Square coupons (25 mm × 25 mm) were cut from 0.5 mm thick Crofer 22 APU commercial sheet stock. Some of the coupons were heat-treated in a tube furnace under flowing argon for either 1 h or 4 h at 1050 °C to modify the initial alloy grain size. This gave three starting conditions for the subsequent oxidation experiments: as-received (AR), heat-treated for 1 h (HT1h) and heat-treated for 4 h (HT4h). The surfaces of all of the coupons were then prepared by first mechanically grinding with 600 and 1200 grit SiC, followed by polishing with 6 μm and then 1 μm diamond slurry to obtain a mirror finish.

The oxidation behavior of the samples was evaluated by thermogravimetric analysis. First, the dimensions of each coupon were measured precisely to establish the starting surface area. Triplicate samples for each of the three starting conditions were mounted in a slotted alumina d-tube so that the samples were standing upright. Oxidation tests were performed in a tube furnace at 800 °C in static laboratory air for up to 750 h. Samples were cooled periodically, removed from the furnace, and weighed using an AT261 Delta Range balance, which has a precision of 0.01 mg.

The effects of pre-oxidation heat treatment and of thermal exposure during oxidation were evaluated by optical microscopy. Cross-sections through the alloy coupons were prepared using standard metallographic techniques and then etched with oxalic acid to reveal the grain boundaries. Grain diameter measurements were taken from optical microscope images using Image Pro Plus 7 image analysis software. The boundary of each grain was traced in the software and the mean diameter tool was used to obtain the average value of diameters drawn through the grain centroid to the points of intersection on the perimeter in 5° increments for each traced grain. The effects of thermal exposure on the room-temperature hardness of the alloy were evaluated by obtaining Vickers microhardness measurements from the metallographic cross-sections using a 500 g load.

One coupon from each heat treatment condition was used for microstructural analysis of the oxide scale. X-ray diffractometry (XRD) was performed using an INEL diffractometer with a solid state Curved Position Sensitive Detector (CPSD), which collects data simultaneously over a 2θ range of 20–140°. The oxidized coupons were mounted flat and scanned for a total of 60 min using a 30 kV Cu K-α source. The data was analyzed using whole pattern fitting with JADE analysis software. Secondary electron (SE) and backscattered electron (BSE) scanning electron microscopy (SEM) images and Energy Dispersive X-ray Spectrometry (EDXS) analyses of the oxide scales formed were obtained in an FEI Helios 600 Dual Beam focused ion beam (FIB) apparatus equipped with a retractable, low kV, segmented BSE detector and an Oxford 80 mm^2 XMax^N Silicon Drift EDXS detector.

Site selective cross-sectional sample preparation for transmission electron microscopy (TEM) was performed using a FEI Strata 400 Dual Beam FIB apparatus equipped with a flip stage for improved final thinning. Firstly, Pt was deposited *in situ* as a capping layer to protect the original surface of the oxide scale. Rough trench milling was performed at an accelerating voltage of 30 kV with a 2.8 nA ion beam current. Samples were lifted out in

situ using an Omniprobe Autoprobe 200 and attached to a TEM grid using Pt deposited via the ion beam. The Ga$^+$ beam currents were successively reduced to 9.5 pA to eliminate milling artifacts in the final specimens. TEM analysis was performed using a Philips CM-200 Supertwin operating at an accelerating voltage of 200 kV and equipped with an EDAX 30 mm^2 Si(Li) detector for EDXS.

3. Results

3.1. Effect of heat treatment on alloy microstructure and hardness

The grain structures corresponding to the three heat treatment conditions (AR, HT1h, HT4h) were evaluated before and after oxidation by optical microscopy on metallographic cross-sections. Representative images are shown in Fig. 1: Fig. 1 (a), (c) and (e) are examples of the grain structures exhibited before oxidation by the AR, HT1h and HT4h coupons, respectively; Fig. 1 (b), (d) and (f) are the corresponding structures for the coupons oxidized at 800 °C for 750 h. Values of the grain diameter were obtained from these samples by taking the mean of the mean diameter value for 30–250 individual grains depending upon the sizes of the grains. The grain diameters for the three samples before oxidation were 15.9, 73.7 and 248.6 μm for the AR, HT1h and HT4h coupons, respectively. Thus, the pre-oxidation heat treatment had the intended effect of growing the grains significantly to produce three rather different starting grain sizes. There was also significant grain growth during the oxidation for the AR and HT1h samples, but not the HT4h sample. The grain diameter for the AR sample after oxidation at 800 °C for 750 h was 90.2 μm; this corresponds to a six fold increase in grain diameter over the unexposed AR sample. For the HT1h samples, both the initial and final grain diameters were larger than those for the AR samples, but the final grain diameter of 192.7 μm was less than three times the

initial value. For the HT4h condition the final grain diameter was 244.1 μm, which is very similar to the initial value for this material.

These changes in grain structure were not accompanied by a reduction in hardness. The mean values of Vickers microhardness obtained from each of the metallographic sections in Fig. 1 are shown in Table 2. In each case these represent the mean of 5 measurements. These values show a small increase in the hardness of the unoxidized samples with heat treatment, and the hardnesses of the oxidized AR and HT1h samples are higher than those of the corresponding unoxidized samples. There was no change in the hardness of the HT4h sample upon oxidation.

3.2. Oxidation kinetics

From the thermogravimetric data it was found that, in each case, parabolic oxidation behavior was established after an initial transient. This is revealed most clearly in plots of weight gain squared against time, as shown in Fig. 2. Each of the sets of samples show a variation in the rate of weight gain up to 250 h, after which weight gain squared varies linearly with time. This is what one would expect from Wagner's theory of parabolic oxidation

$$(w/A)^2 = k_g t$$

where w is the weight gain, A is the specimen surface area, k_g is the parabolic rate constant, and t is the oxidation time. Using the linear portions of the plots from 250 h to 750 h we obtained values of $k_g = 4.8 \times 10^{-8}$, 2.8×10^{-8} and 1.4×10^{-8} mg^2 cm^{-4} s^{-1} for the AR, HT1h and HT4h samples, respectively. We note that this reduction in k_g is very significant and indeed this is comparable to the values obtained by applying MCO coatings to Crofer 22 APU in our previous studies ($k_g = 1.45 \times 10^{-8}$ mg^2 cm^{-4} s^{-1} at 800 °C [17]). The
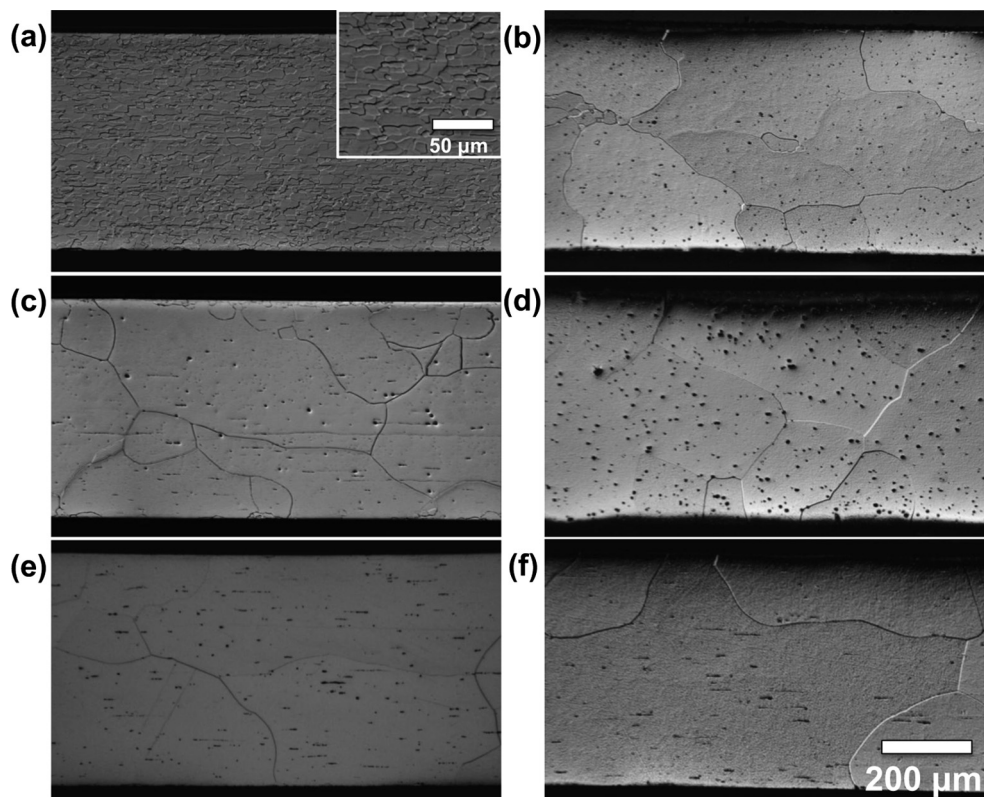

Fig. 1. Optical micrographs showing etched metallographic sections through coupons of the AR (a,b), HT1h (c,d) and HT4h (e,f) materials; (a), (c) and (e) are coupons before oxidation whereas (b), (d) and (f) are coupons oxidized at 800 °C for 750 h.

Table 2
Mean values of Vickers microhardness measurements obtained from the metallo-
graphic cross-sections shown in Fig. 1.

	AR	HT1h	HT4h
Unoxidized	138	148	155
Oxidized	148	149	155

microstructural data presented below were acquired to reveal the
origins of this improvement in oxidation resistance.

3.3. Plan view characterization of oxide scales (XRD and SEM)

The X-ray diffraction data obtained from the oxidized AR, HT1h
and HT4h coupons are shown in Fig. 3. Peak fitting using the ICDD
database indicated that the major phases present in each case are
rhombohedral Cr_2O_3, cubic $MnCr_2O_4$ spinel and body-centered-
cubic α-Fe. The relative intensities of the peaks were used to esti-
mate the volume fractions of the phases, and the values obtained
were: 63% $MnCr_2O_4$, 32% Cr_2O_3 and 5% α-Fe for the AR sample; 65%
$MnCr_2O_4$, 30% Cr_2O_3 and 5% α-Fe for the HT1h sample; and 79%
$MnCr_2O_4$, 14% Cr_2O_3 and 7% α-Fe for the HT4h sample.

The distribution of these phases was inferred from SEM analysis
on the surfaces of the oxide scales. Representative BSE SEM images
obtained from the AR, HT1h and HT4h coupons oxidized at 800 °C
for 750 h are shown in Fig. 4. In each case the scale is comprised of
larger octahedral crystals with smaller particles having a less well-
defined morphology between these octahedra. Qualitative EDXS
data indicate that the large octahedra are the $MnCr_2O_4$ phase, the
finer particles are the Cr_2O_3, and that there are no isolated regions
of exposed α-Fe. Thus, the presence of α-Fe peaks in the XRD data
must correspond to contributions from the underlying Crofer
substrate. The main differences between the oxide scales for the
three samples are the dimensions and coverage of the $MnCr_2O_4$
octahedra; the sizes of these features were 0.3–1.5 μm for the AR
sample, 0.8–2.1 μm for the HT1h sample and 0.9–3.8 μm for the
HT4h sample. It is difficult to estimate the $MnCr_2O_4$ coverage
accurately from such images but it is clear that this phase consti-
tutes a larger proportion of the exposed surface area of the scale for
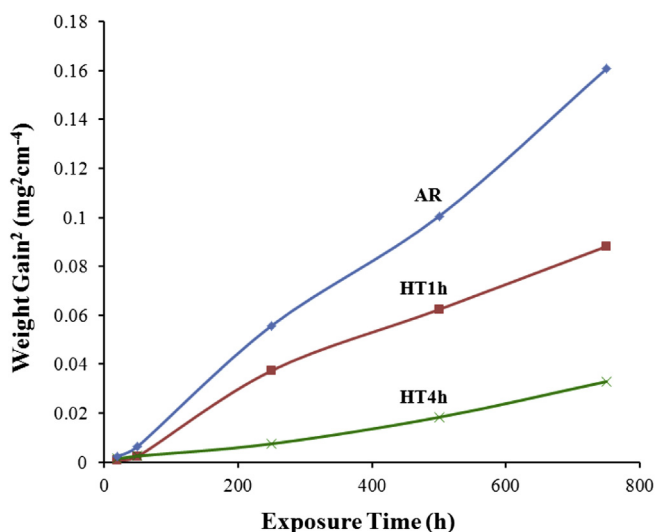the HT4h sample than for the AR or HT1h samples.

Fig. 2. Plot of parabolic weight gain (mg² cm⁻⁴) vs. exposure time for samples exposed
in static air at 800 °C. The gravimetric rate constants (k_g) measured from the linear
region between 250 h and 750 h were 4.82×10^{-8} mg² cm⁻⁴ s⁻¹,
2.82×10^{-8} mg² cm⁻⁴ s⁻¹ and 1.41×10^{-8} mg² cm⁻⁴ s⁻¹ for the AR, HT1h and HT4h
samples, respectively.

3.4. TEM microstructural and chemical analysis of oxide scales

The details of the scale microstructures were revealed using
TEM and STEM analyses of FIB-cut cross-sections through the
scales. Examples of the TEM and STEM data obtained from the AR
sample oxidized at 800 °C for 750 h are shown in Figs. 5 and 6,
respectively. Fig. 5 (a) is a bright field TEM image of the scale
morphology and Fig. 5(b)–(d) are representative selected area
diffraction patterns (SADPs) obtained from the three distinct
microstructural regions in the scale labeled 1, 2 and 3, respectively
in Fig. 5(a). Region 1 is a coarse grained outer layer and the SADPs
obtained from these grains correspond to those expected for a cubic
spinel phase having a lattice parameter of $a_0 = 0.836$ nm. The EDXS
data obtained from such grains are consistent with this phase being
$MnCr_2O_4$ with a small amount (1–3 wt.%) of Fe. Region 2 is a fine-
grained layer below the $MnCr_2O_4$. The grains are too small for the
acquisition of single crystal zone axis SADPs, but all of the diffrac-
tion spots in patterns such as Fig. 5(c) lie on rings corresponding to
strongly diffracting planes in Cr_2O_3 with the corundum structure
($a_0 = 0.496$ nm, $c_0 = 1.359$ nm). The EDXS measurements obtained
from this layer indicated that this chromia layer contained
approximately 1 wt.% Ti. Region 3 is an example of a subscale oxide
pocket that protrudes into the substrate from the chromia/alloy
interface. The SADPs and EDXS data obtained from such pockets
indicated that, like region 1, these were cubic $MnCr_2O_4$ spinel with
a small amount of Fe incorporated into the lattice, although in these
cases the Fe content was less than 1 wt.%.

The distribution of the phases in the scale for the AR sample was
rather inhomogeneous. To show this more clearly, STEM X-ray
maps were acquired from the FIB-cut sections. Fig. 6 is an example
of these data obtained from approximately the same region as
Fig. 5; this comprises a BF STEM image of the region analyzed
together with maps for Cr, Mn, Fe, O and Ti. Each map corresponds
to a grid of 256×200 measurements of the counts within a 100 eV
window centered on the $K\alpha_1$ energy for that element. The data
were acquired by scanning the region 2048 times with a dwell time
of 0.2 ms per measurement for a total acquisition time of around
5.8 h corresponding to just over 0.4 s per pixel. From the Cr and O
maps, it is clear that the thickness of the Cr_2O_3 scale varies from
approximately 250 nm on the right-hand side of the mapped region
to over 3 μm on the left. Such observations revealed that the Cr_2O_3
scale was thinner in the regions where external $MnCr_2O_4$ spinel
was present. The regions between the $MnCr_2O_4$ exhibited a much
thicker Cr_2O_3 scale with embedded Fe-rich pockets. The composi-
tion of these pockets measured by EDXS was consistent with the
bulk composition of Crofer 22 APU. The Ti and O maps show a very
finely dispersed internal oxide phase forming below the Cr_2O_3 scale
within the Fe–Cr matrix. The Mn and Cr maps clearly reveal the
presence of $MnCr_2O_4$ subscale spinel pockets 500–1000 nm in
diameter between the Cr_2O_3 scale and the Crofer substrate. We note
that while the chemistry and crystal structure of the inner and
outer $MnCr_2O_4$ are rather similar, there is a clear difference in
morphology: the subscale spinel pockets are more equi-axed,
whereas the outer spinel layer exhibits pronounced crystallo-
graphic facets.

Representative bright field TEM images obtained from FIB-cut
cross-sections through the oxidized HT1h and HT4h samples are
shown in Fig. 7. In both cases, the same three microstructural re-
gions (outer $MnCr_2O_4$, Cr_2O_3 layer and subscale $MnCr_2O_4$ pockets)
were observed in the oxide scale, but the layers/regions were
thinner and distributed more homogeneously than for the AR
sample. As such, quantitative EDXS line-scans were acquired
(rather than more qualitative X-ray maps such as Fig. 6) and ex-
amples from the oxidized HT1h and HT4h samples are shown in
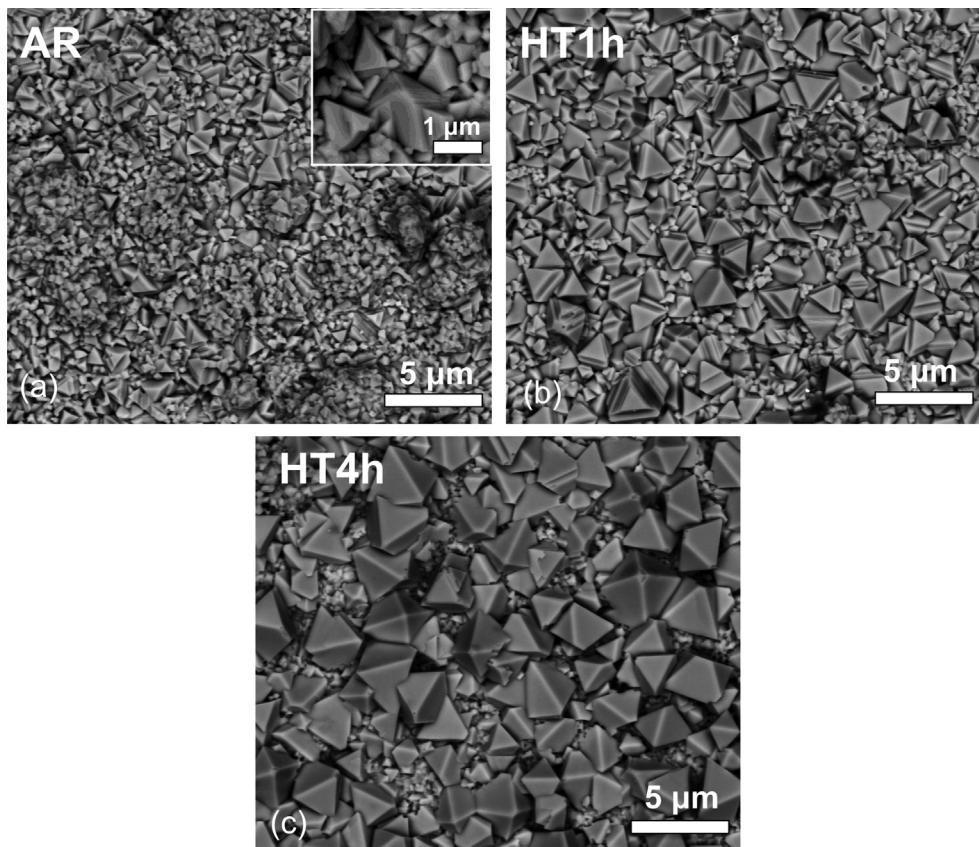Figs. 8 and 9, respectively.

Fig. 3. Plan view BSE SEM images of the oxide scale surface for samples oxidized for 750 h at 800 °C: (a) AR, (b) HT1h and (c) HT4h.

Fig. 8(a) is an annular dark field (ADF) STEM image obtained from the FIB-cut cross-section of the oxidized HT1h sample with the alloy on the left-hand side of the image and the oxide scale on the right. Fig. 8(b) is a compositional profile determined from EDXS measurements obtained along the bright horizontal line indicated in Fig. 8(a). Spectra were acquired at 10 nm intervals along the line using a 10 nm diameter electron probe with an acquisition time of 3 s per spectrum. The integrated intensities in the K peaks for each of the elements were used to perform a standard-less

quantification of the data based upon the thin film approximation. The first 500 nm of the linescan plot in Fig. 8 corresponds to the Crofer with a measured chemistry of 78 wt.% Fe and 22wt.% Cr. The chromia scale in this location is around 375 nm thick and this contains a small amount (≈ 0.5wt.%) of Ti. It should be noted that while the chromia scale in this particular area is quite thin, other regions such as those shown in Fig. 7(a) are much thicker; Cr_2O_3 layer thicknesses of 300–1200 nm were measured for the HT1h sample. The chemistry for the last 1.5 μm of the linescan shown in Fig. 8 is consistent with the $MnCr_2O_4$ spinel phase. We note that the Fe content in the spinel increases from approximately 1.5 wt.% at the chromia/spinel interface to 4.5 wt.% towards the surface of the spinel.

The corresponding data obtained from the oxidized HT4h sample is shown in Fig. 9. The first 1 μm of the linescan corresponds to the alloy composition. The next 100 nm is representative of a subscale $MnCr_2O_4$ pocket similar to those observed on the AR sample. The chromia scale in this particular region is approximately 650 nm thick and again contains approximately 0.5 wt.% Ti. Here again, there was significant variation in the thickness of the chromia layer. Indeed, the area shown was the thickest region observed, and in most places the chromia scale was 100–550 nm thick. The final 1.2 μm of the linescan are again consistent with $MnCr_2O_4$ spinel, however the Fe content ranges from about 1.0 wt.% near the chromia/spinel interface up to 2.5 wt.% near the surface of the spinel.

3.5. Characterization of internal oxidation

As shown in Fig. 6, there are Ti-rich internal oxides within the Crofer 22 APU substrate below the $MnCr_2O_4/Cr_2O_3$ scale. These
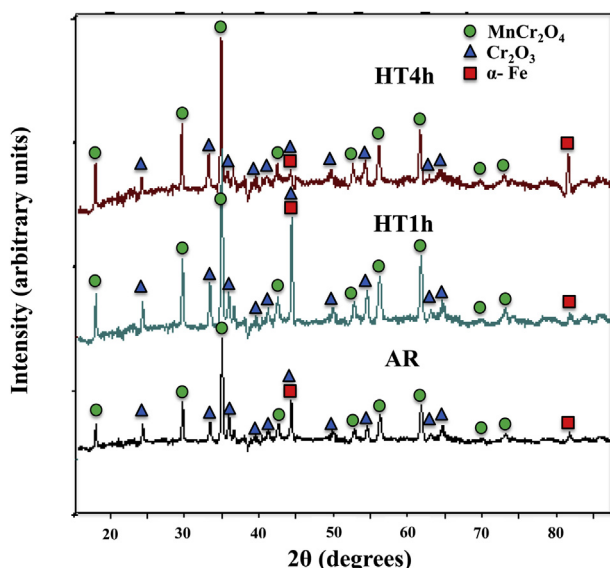

Fig. 4. XRD data obtained from the surface of samples oxidized for 750 h at 800 °C.
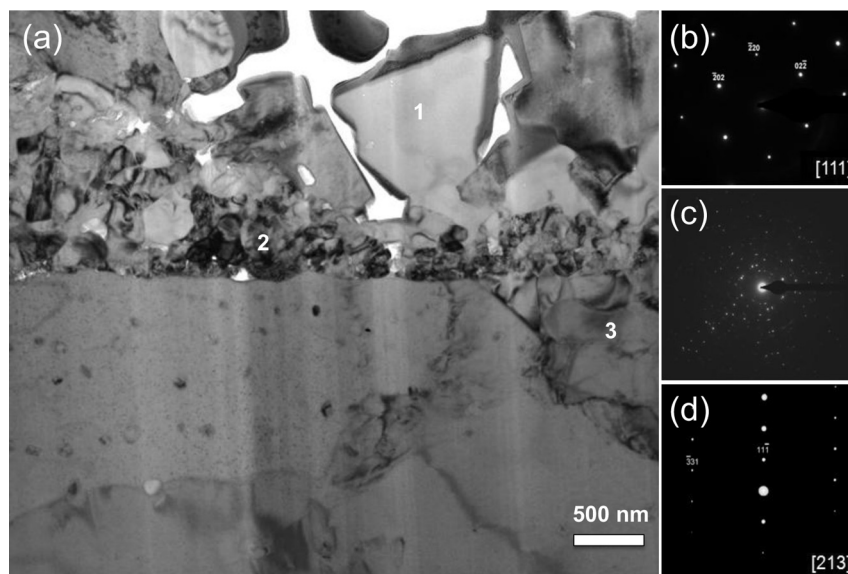
Fig. 5. TEM data acquired from a FIB-cut cross section through the surface of an AR sample oxidized for 750 h at 800 °C: (a) BF TEM image; (b), (c) and (d) SADPs from regions 1, 2 and 3 in (a), respectively. The single crystal zone axis patterns in (b) and (d) correspond to a cubic spinel phase whereas the spotty ring pattern in (c) is consistent with the corundum structure of Cr_2O_3.

internal oxides are extremely fine (≈ 50 nm) in the case of the AR sample, but are up to 300 nm in diameter in the oxidized HT4h sample. While accurate quantitative analysis was challenging for such embedded particles due to interference from the surrounding metallic matrix and to an overlap of the O-K and Ti-L peaks, an average of EDXS measurements taken from the three largest internal oxides gave an O:Ti ratio of 2.28. Since the highest oxidation state for titanium is +4, the obvious conclusion is that these internal oxides are TiO_2, but this was not borne out by the electron diffraction data. Fig. 10 is a BF image from a region in the oxidized HT4h sample that contains two such internal oxide particles, and the inset is a zone axis SADP from one of these particles. All of the particles appeared to be single crystal, but the lattice spacings obtained from the SADPs were not consistent with any of the three known polymorphs of TiO_2 (anatase, brookite or rutile). Indeed the only known Ti-O phase that appeared to match the measured lattice spacings is the low-temperature monoclinic polymorph of TiO identified by Watanabe et al. [18] (space group $A2/m$, $a_0 = 0.585$ nm, $b_0 = 0.934$ nm, $c_0 = 0.414$ nm).

3.6. Short-term oxidation studies

Although the observations on samples oxidized for 750 h revealed significant differences between the oxide scales for the three alloy conditions, there was no obvious mechanistic link between these features and the measured change in parabolic rate constant. To investigate this phenomenon further, additional samples were prepared and oxidized under the same conditions, but the samples were withdrawn for microstructural analysis after just 5 h.

Fig. 11(a) is a low voltage (2 kV) SE SEM image of the scale formed on the AR sample after 5 h of oxidation. At this stage, there are already large (300–650 nm) faceted spinel particles that partially cover a fine-grained chromia scale, and the arrangement of these particles suggests strongly that they have formed preferentially at locations where the alloy grain boundaries intersect the surface. To verify this, SE SEM images were obtained from the polished face of FIB-milled trenches cut into the sample surface. One such image is shown in Fig. 11(b). The chromia scale is just 30–
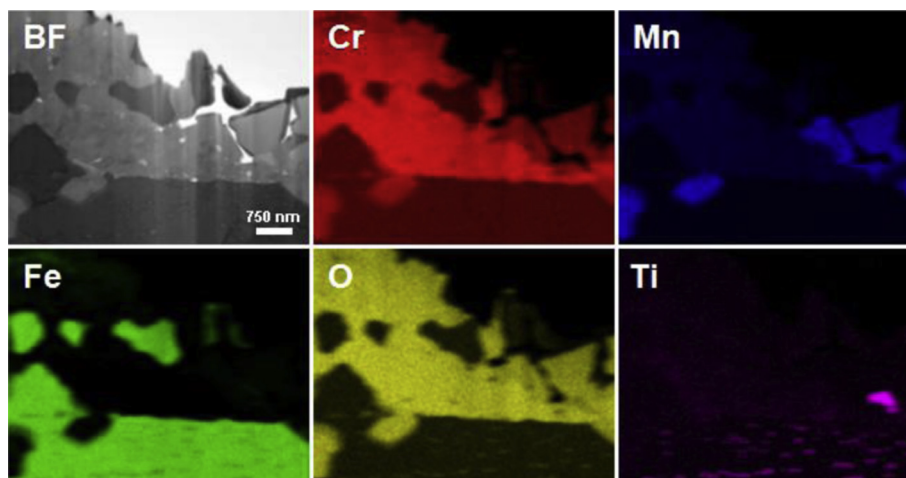

Fig. 6. STEM data acquired from a FIB-cut cross section through the surface of an AR sample oxidized for 750 h at 800 °C. The BF image shows the region analyzed and the X-ray maps show the integrated intensities in 100 eV windows centered on the $K\alpha_1$ energies for each element.
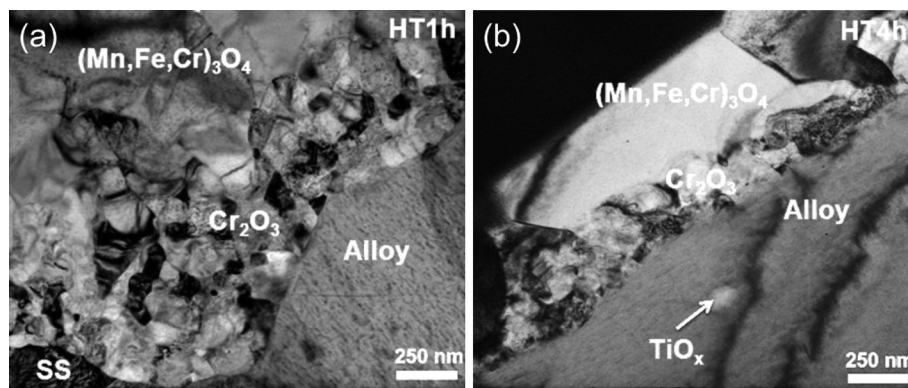
Fig. 7. BF TEM images acquired from a FIB-cut cross section through the surface of samples oxidized for 750 h at 800 °C: (a) HT1h, (b) HT4h.

50 nm thick in such regions and it is clear that a large spinel particle lies at the point where a grain boundary in the alloy intersects the surface. The chemistry of the oxide scale is revealed most clearly in X-ray maps obtained from the sample surfaces, and one example is shown in Fig. 12. This comprises an SE SEM image and maps for Cr, Fe, Mn, O and Ti. Each map corresponds to a grid of 512×400 spectra acquired over an area of 26.6×20.8 μm. Due to the extremely high count rate for the SDD EDXS detector (150,000 counts s^{-1}) full spectral information could be acquired in a single scan with a dwell time of 3 ms per pixel, corresponding to a total acquisition time of 10 min. Unlike the STEM maps shown in Fig. 6, the map intensities shown here are proportional to the corresponding compositions obtained from quantitative analysis of the spectra. The maps show strong enhancement of Cr, Mn and O at the boundaries consistent with the preferential formation of MnCr$_2$O$_4$ at these locations. The Fe map shows a complementary trend; this

is consistent with the Fe signal arising from the underlying alloy being strongly excited through the thinner chromia scale but less so through the thicker spinel at the emergent alloy grain boundaries.

Corresponding data from the HT4h sample after 5 h of oxidation are shown in Figs. 13 and 14. The polyhedral spinel particles are present on the surface of the scale as shown in Fig. 13(a), but the particles are smaller (175−500 nm) and cover less of the alloy surface area than for the AR sample (Fig. 11(a)). SE SEM images such as Fig. 13(b) obtained from FIB-cut cross-sections show a much thicker chromia scale (90−275 nm). Since the alloy grain size is far larger than the field of view in such images, no grain boundaries were observed in such sections, however examples of the faceted spinel particles were still present in such region. The distribution of the spinel particles was revealed clearly in SE SEM images and X-ray maps obtained from the sample surfaces (e.g. Fig. 14). These
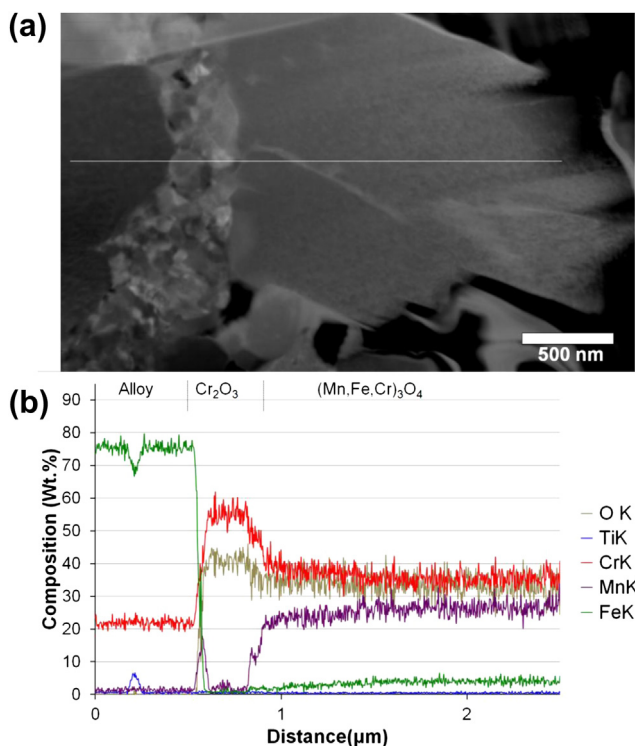

Fig. 8. STEM data acquired from a FIB-cut cross section through the surface of an HT1h sample oxidized for 750 h at 800 °C: (a) BF image; (b) compositional profile obtained from spectra acquired at points along the horizontal line in (a).
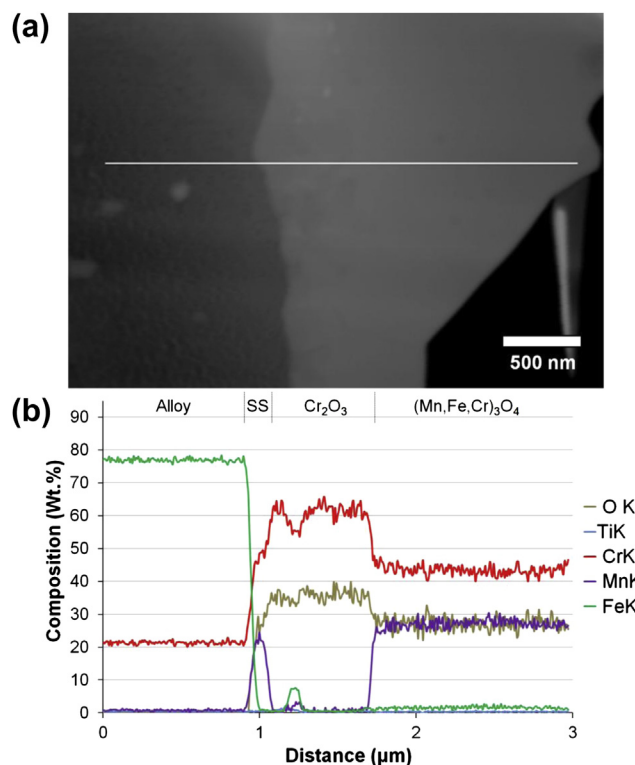

Fig. 9. STEM data acquired from a FIB-cut cross section through the surface of an HT4h sample oxidized for 750 h at 800 °C: (a) BF image; (b) compositional profile obtained from spectra acquired at points along the horizontal line in (a).
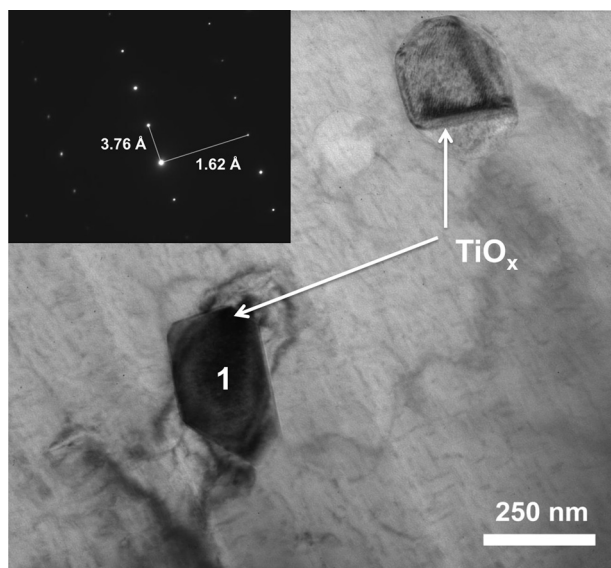
Fig. 10. Bright field TEM image showing internal oxides in an HT4h sample oxidized for 750 h at 800 °C. The inset is an SADP taken from the oxide particle labeled "1".

spinel particles are dispersed much more homogeneously across the alloy surface than for the AR sample shown in Fig. 12.

4. Discussion

It is clear from the data presented in the previous section that the heat treatment of Crofer 22 APU has a profound effect on the oxidation kinetics and on the microstructural development of the oxide scale. In the sections that follow we discuss the possible mechanisms involved in the development of these microstructures and their implications for long-term SOFC durability. Firstly, we consider the way in which the microstructure develops on the AR samples. The effects of pre-oxidation heat treatment are then discussed. These observations are compared to our previous studies on MCO-coated Crofer 22 APU, and finally the implications of these observations for SOFC performance are noted.

4.1. Microstructure and scale development of AR Crofer 22 APU

The main microstructural features observed in the oxide scales that develop on the AR samples are a continuous Cr_2O_3 layer in contact with the alloy substrate and a discontinuous $MnCr_2O_4$ layer

on top of the Cr_2O_3. There are also two types of internal oxides: $MnCr_2O_4$ pockets which form between the alloy substrate and the Cr_2O_3 scale, and small (≈ 50 nm) equi-axed Ti-rich oxide precipitates. In addition to these various types of oxides there are metallic inclusions within the Cr_2O_3 scale for the AR samples.

There are numerous examples in the literature of ferritic stainless steels that form two-layer oxide scales, and the alloy that has received the most attention is SS 430 [19–21]. Such Fe–Cr–Mn alloys form an initial Cr_2O_3 layer very rapidly during oxidation. Saeki used a combination of X-ray photoelectron spectrometry and XRD to characterize the oxides formed on SS 430 in O_2/N_2 at 1000 °C for up 20 min Ref. [20]. It was found that during the first 15–30 s of oxidation, only a single-phase oxide layer with the corundum structure is present. Initially this layer has a chemical composition close to Fe_2O_3, but this changes rapidly to Cr_2O_3. After 30 s of oxidation an $MnCr_2O_4$ spinel phase was observed which also corresponded to a change in the oxidation state of Mn from +3 (Mn_2O_3) to +2 ($MnCr_2O_4$). It was proposed that the induction period for the formation of the spinel corresponded to the time taken for Mn_2O_3 to reach its maximum solubility in Cr_2O_3 (12–17 wt.%). Once this value was exceeded, the $MnCr_2O_4$ spinel nucleated on the surface and grew via a reaction between Mn_2O_3 and Cr_2O_3 [19,20]. If this is the mechanism by which the two-phase scale forms on the Crofer 22 APU samples considered in this study then the scale microstructure may be dictated by the initial nucleation rate for the chromia. This is because the nucleation rate will determine the chromia grain size, and grain boundary diffusion of transition metals through Cr_2O_3 is 3–5 orders of magnitude faster than bulk diffusion [22]. Moreover, it has been reported that grain boundary diffusion of Mn is 1–2 orders of magnitude faster than grain boundary diffusion of Cr or Fe in Cr_2O_3 [22,23].

Our observations of the scale formed after just 5 h oxidation of the AR sample (Figs. 11 and 12) indicate that outward Mn and Cr diffusion via chromia grain boundaries is initially extremely rapid, resulting in the formation of a substantial amount of $MnCr_2O_4$ phase. The subsequent growth of the outer spinel layer must be dramatically slower because there are still some unoccluded regions of chromia on the surface after 750 h (Fig. 3). It is interesting to note that in a previous study on high temperature oxidation of Fe–Cr–Mn systems by Cox et al. [24] a change in the parabolic rate constant after a particular exposure time was attributed to the point at which there is complete surface coverage by the Mn–Cr spinel. At this stage the oxidation rate would no longer be solely controlled by outward diffusion of Cr^{3+} through the Cr_2O_3 as it is initially. Although a similar change in parabolic rate constant was observed at 250 h for the AR samples in the current work, this is
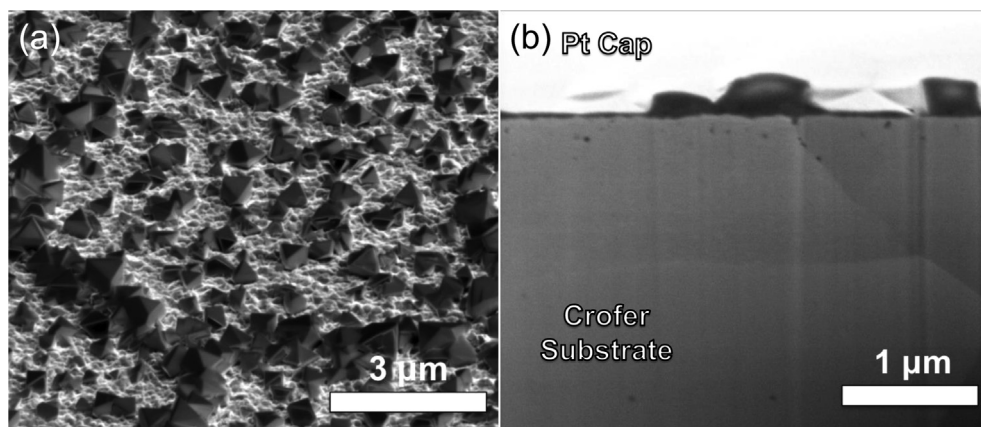

Fig. 11. SE SEM images obtained from an AR sample oxidized for 5 h at 800 °C: (a) morphology of the oxide scale surface; (b) FIB-cut cross-section through the surface.
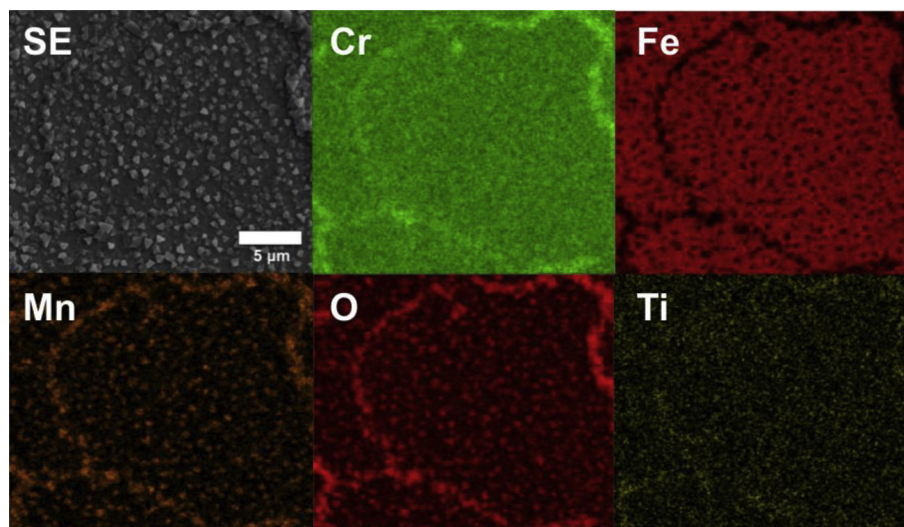
Fig. 12. SEM data obtained from the surface of an AR sample oxidized for 5 h at 800 °C. The SE image shows the region analyzed and the X-ray maps show relative intensities proportional to the local composition of each element from quantitative analysis of EDXS data at each pixel.

clearly not due to spinel coverage alone because complete surface coverage by spinel has not been achieved at this point. Since there is only ≈0.5 wt.% Mn in the alloy, it seems more likely that the change in rate constant at 250 h occurs due to a depletion of the Mn in the alloy. Indeed, a similar change in parabolic rate constant has been observed by Kim et al. [25] on Haynes 230, which is another alloy which forms a two-layer $Cr_2O_3/MnCr_2O_4$ scale. This change in kinetics was attributed to complete oxidation and depletion of the initial Mn source in the alloy. Since the $MnCr_2O_4$ spinel forms preferentially at the emergent alloy grain boundaries, it is clear that Mn diffuses more rapidly along these boundaries than through the grains as one might expect. Thus the alloy grain size would dictate the total oxidation time required to deplete the Mn. Beyond this point, the measured oxidation kinetics are presumably dominated by the transport of chromium through the alloy and the scale.

The subscale $MnCr_2O_4$ pockets observed in this study are similar to those found in our previous study on MCO-coated coated Crofer 22 APU [11] and in numerous other studies on similar alloy systems [24,26,27]. Cox et al. proposed that this subscale spinel phase may be formed during the early stages of oxidation due to vacancy coalescence and void formation below the chromia scale. Such voids could cause the thin chromia scale to crack, exposing the

underlying alloy to the oxidizing atmosphere. The local increase in O_2 partial pressure in a region depleted in Cr may favor the formation of $MnCr_2O_4$ [24]. This mechanism would lead to the majority of these subscale pockets being formed during the earliest stages of oxidation when the chromia scale is still quite thin. We note that in the current study the subscale spinel pockets were observed even after 5 h exposure, and that they showed a propensity to form near alloy grain boundaries.

The formation of Ti-rich internal oxides in the AR samples during oxidation is consistent with a previous report by Froitzheim et al. [28] on oxidation microstructures for related Fe–Cr–Mn alloys oxidized at 1000 °C in laboratory air. In this previous study, it was concluded that the internal oxides were probably Ti_2O_3 and/or Ti_3O_5. In the present case, the electron diffraction data are not consistent with either of these phases or indeed any of the known polymorphs for TiO_2, despite this being the stoichiometry suggested by the EDXS data. The SADPs instead correspond to the monoclinic polymorph of TiO first identified by Watanabe et al. [18]. This structure is a defect analog of the NaCl-type structure and can be produced from the parent structure by ordering of approximately 15% vacancies on the lattice sites of the cubic parent structure (e.g. Ref. [29]). Due to the defect character of the structure, it can accommodate significant deviations from stoichiometry
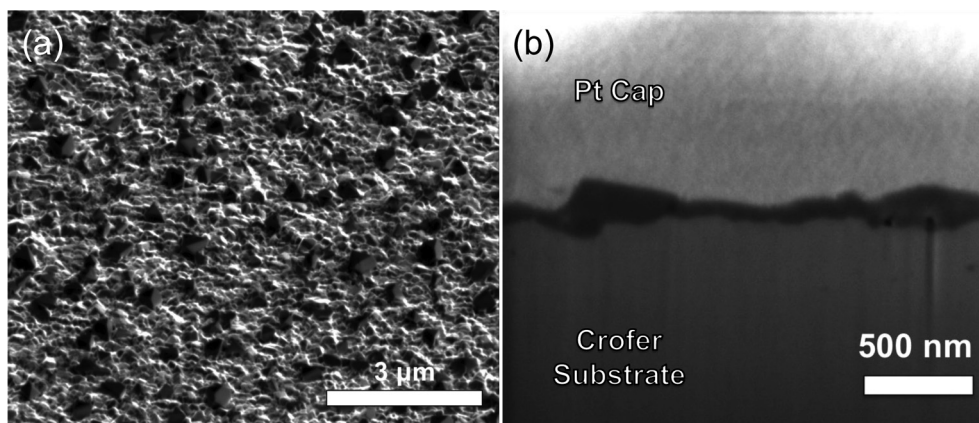

Fig. 13. SE SEM images obtained from an HT4h sample oxidized for 5 h at 800 °C: (a) morphology of the oxide scale surface; (b) FIB-cut cross-section through the surface.
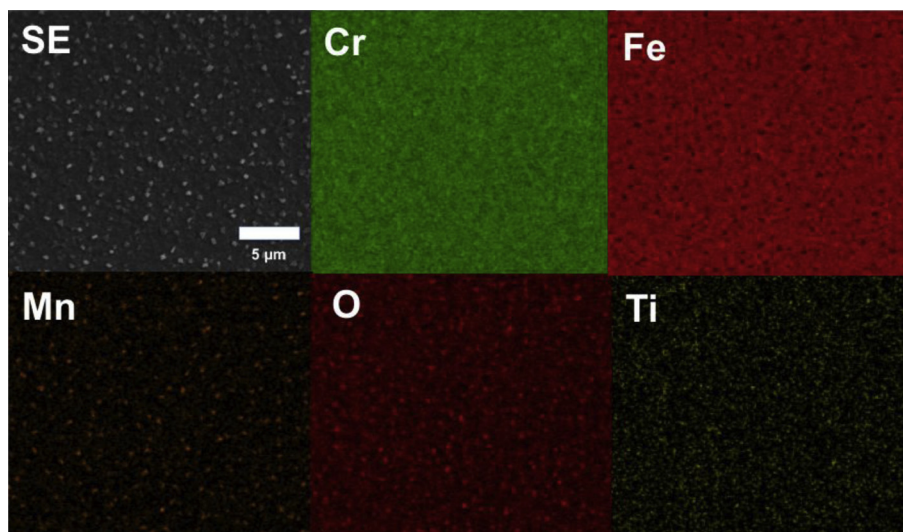
Fig. 14. SEM data obtained from the surface of an HT4h sample oxidized for 5 h at 800 °C. The SE image shows the region analyzed and the X-ray maps show relative intensities proportional to the local composition of each element from quantitative analysis of EDXS data at each pixel.

giving compositions TiO_x with $x = 0.7$–1.25. We note that while the measured compositions for the internal oxides fall well outside this range, there is considerable uncertainty in the measurements due to the size of the particles and to an overlap of the O-K and Ti-L peaks.

The metallic inclusions/protrusions observed in the chromia scale (e.g. Fig. 6) are similar to those reported elsewhere in the literature for various alloy systems [14,26,27,30,31]. All of these previous works attribute the metallic inclusions to stresses that arise from internal oxidation of titanium or the formation of $MnCr_2O_4$ subscale pockets. Issartel et al. accounted for these stresses on the basis of the Pilling-Bedworth ratio for these internal oxidation reactions [31]. They showed that a combination of compressive stresses in the oxide, tensile stresses in the alloy, and small pre-existing undulations on the alloy surface could lead to extrusion of the metal into the scale adjacent to internal oxides in SS 439 and SS 441 [31]. Our observations of metallic protrusions forming directly between $MnCr_2O_4$ subscale spinel pockets, such as in Fig. 6, are consistent with this mechanism. While these metallic protrusions may provide "keying" or interlocking with the oxide scale during short-term exposure studies, they could potentially be detrimental during long-term exposure, as they would act as stress-risers and potential sites for localized scale spallation.

4.2. Effect of pre-oxidation heat treatment on oxidation kinetics and microstructure

The most obvious effect of the pre-oxidation heat treatment of the Crofer 22 APU at 1050 °C in argon is the growth of the initial alloy grain size from an average of 15.9 μm in the AR sample to 73.7 μm and 248.6 μm in the HT1h and HT4h samples respectively. While the AR and HT4h samples exhibit fairly consistent grain sizes through the coupon thickness, the HT1h sample clearly has finer grains at the surface than within the center of the coupon. There are two main ways in which such an anisotropic grain size distribution could arise. Firstly, grain boundary/surface interactions could inhibit the growth of near-surface grains, leading to a smaller grain size at the surface during the initial stages of grain growth. Secondly, if the dislocation densities at the surface are higher than within the bulk of coupons then the near-surface grains could undergo recrystallization prior to grain growth while recovery and

grain growth processes operate throughout the remainder of the material. Although the latter processes would seem to be the best explanation for the observed grain structure, we note that the AR sheet stock is provided in the recovered/annealed condition and so the residual defect density should be too low for recrystallization to occur. It is interesting to note that there is no softening of the alloy associated with the dramatic grain growth during the pre-oxidation heat treatment or during the oxidation experiments. This is presumably because the effects of dispersion hardening from the Ti-rich internal oxides are more than enough to compensate for the reduction in Hall-Petch strengthening.

The main features of the oxide scale microstructures on the HT1h and HT4h samples are the same as for the AR samples. Thus, there is a continuous Cr_2O_3 layer on the alloy with an outer discontinuous $MnCr_2O_4$ spinel layer, subscale pockets of $MnCr_2O_4$, and Ti-rich internal oxide precipitates in the alloy below the scale. It should be noted that the Ti-rich internal oxides are present in the unoxidized HT1h and HT4h samples, as seen in Fig. 1. Since these internal oxides must form due to oxygen pick-up during heat treatment, the contribution of such oxides to the total weight gain would not be incorporated into the thermogravimetric measurements. While this effect might lead to an underestimate of the total weight gain, even if all of the Ti were consumed in the formation of such internal oxides then this would only account for a small proportion of the difference in k_g between the AR and HT4h samples. The presence of around 0.5% Ti in the chromia demonstrates that there must be a lower volume fraction of TiO_x than this analysis would imply and so we can neglect this effect as a major cause of the differences in the measured values of k_g.

The most significant difference between the scale microstructures for the AR and the HT1h and HT4h samples is in the size and coverage of the outer spinel layer. The outer $MnCr_2O_4$ grains were 0.3–1.5 μm for the AR sample, 0.8–2.1 μm for the HT1h sample, and 0.9–3.8 μm for the HT4h sample (Fig. 3). Coverage was difficult to measure accurately, but the XRD analysis showed an increase in the proportion of the volume sampled that corresponded to $MnCr_2O_4$ from 63% in the AR sample to 65% for HT1h and 79% for HT4h. The way in which these differences arise can be inferred from the microstructures of the scales formed on the AR and HT4h samples after just 5 h oxidation at 800 °C. It is clear that the chromia scale on the AR sample is much thinner than that on the HT4h sample after

5 h. This would indicate that the Cr_2O_3 nucleation rate was higher on the AR sample, leading to a finer-grained chromia scale during initial oxidation. In addition, the finer alloy grains in the AR sample would allow for more rapid transport of Mn to the surface of the alloy where it would react to form $MnCr_2O_4$, thereby depleting the reservoir of Cr available to form Cr_2O_3. Initially this thinner chromia scale leads to the formation of larger and more numerous $MnCr_2O_4$ nuclei on the AR sample. After 750 h oxidation, however, the smaller nuclei on the HT4h sample had grown into larger spinel grains covering more of the sample surface. Since the long-term oxidation kinetics are dominated by grain boundary diffusion through the Cr_2O_3 and $MnCr_2O_4$, the larger outer spinel grains formed on the HT4h sample would provide fewer preferential diffusional paths for oxygen ingress and/or chromium egress. This is presumably the reason why the HT4h samples exhibited a $3.5\times$ lower value of k_g than the AR samples.

4.3. Comparison of bare and MCO-coated Crofer 22 APU

In previous studies by the current authors it was found that oxidation of MCO-coated Crofer 22 APU in air led to the formation of scales with many similar features to those observed in this study [11,17]. Thus, the coated samples formed: continuous chromia scales at the alloy/coating interface, subscale $MnCr_2O_4$ pockets and equi-axed internal TiO_x precipitates. Since these phases also form in the absence of an MCO coating, they are clearly inherent to the oxidation of Crofer 22 APU. In the MCO-coated alloy, however, a thick ($\approx 5\ \mu m$) reaction layer (RL) formed between the Crofer 22 APU and the MCO after 1000 h oxidation at 800 °C, resulting in a $5.5\times$ reduction in k_g compared to bare (as-received) Crofer 22 APU [17]. The details of the complex RL formed on MCO-coated Crofer 22 APU were recently studied in greater detail [11], and it was observed that after 1000 h oxidation at 800 °C the RL comprised a cubic spinel with a chemistry of $Mn_{1.38}Co_{0.84}Cr_{0.54}Fe_{0.24}O_4$ [11]. While it is thermodynamically favorable to form an $MnCr_2O_4$ outer spinel on bare Crofer 22 APU, the presence of the $(Mn, Co, Cr, Fe)_3O_4$ RL in direct contact with Cr_2O_3 indicates that this mixed RL spinel is more thermodynamically stable than $MnCr_2O_4$ in the MCO-coated Crofer system. It has been previously proposed by Fergus et al. that the RL grows by concurrent inward migration of the RL/Cr_2O_3 and Cr_2O_3/alloy interfaces [32,33]. Additional work is necessary to determine how alloy heat treatment may impact the thickness and chemistry of the RLs formed between Crofer 22 APU and MCO, however it is tempting to speculate that the alloys subjected to a pre-oxidation heat treatment, which resulted in a greater volume of $MnCr_2O_4$ outer spinel, may indeed produce thicker RLs.

4.4. Implications for SOFC performance

The benefits of utilizing an alloy that forms an $MnCr_2O_4$ outer spinel scale have been shown previously in a study by Yang et al. [12] in which a decrease in area specific resistance (ASR) was observed for such alloys as compared to ferritic stainless steels that form single-layer chromia scales. This drop in resistance was attributed to the $MnCr_2O_4$ impeding the ingress of oxygen and limiting the underlying growth of the chromia scale. We observed a similar phenomenon in the EDXS maps such as Fig. 6, which show a substantially thinner Cr_2O_3 scale being formed below the $MnCr_2O_4$ outer spinel than in the exposed regions. Stanislowski et al. [2] showed that alloys such as Crofer 22 APU, which form outer $MnCr_2O_4$ layers, exhibit 60–70% less chromia volatility than pure chromia formers such as Ducrolloy. However, it was also shown that Cr can still diffuse rapidly through the $MnCr_2O_4$ thus replenishing the source for evaporation of chromium species. It was concluded that the reduction in chromia volatility for alloys with two-layer chromia/spinel scales was solely due

to the lower partial pressure of volatile chromia species that form over $MnCr_2O_4$ as compared to that over Cr_2O_3.

Although $MnCr_2O_4$ may be effective at retarding oxidation rates and inhibiting the egress of volatile chromium species, the electrical conductivity at 800 °C is still rather low ($0.004-0.08$ S cm^{-1} [34,35]). It is unclear what effect the substitution of small amounts of Fe into $MnCr_2O_4$, as observed in the present study, would have on electrical conductivity. It seems likely that the RL formed on MCO-coated Crofer 22 APU has a much higher conductivity than the $MnCr_2O_4$ formed on the bare alloy. Wang et al. [33] measured the conductivities of spinels with chemistries similar to the RL reported previously by the current authors [11] and obtained a value of 22.2 S cm^{-1}. We note that the RL reported in our previous work contained a small amount of Fe, while the spinels studied by Wang et al. contained only Mn, Cr and Co; thus additional conductivity measurements are needed to evaluate the properties of the RLs formed on MCO-coated Crofer 22 APU systems.

We note that the RL formed on MCO-coated Crofer 22 APU appears to be beneficial in slowing down oxidation kinetics as proposed in the model developed by Chen et al. [17]. The current work shows that pre-oxidation heat treatment of Crofer 22 APU not only reduces the parabolic oxidation constant by $3.5\times$ but also promotes the formation of additional $MnCr_2O_4$ as compared to the AR samples. Thus, heat treatment of the alloy prior to MCO coating might result in a thicker RL, which would further reduce the oxidation rate for Crofer 22 APU. The combined effects of alloy heat treatment and a protective spinel coating have not yet been studied, but this approach could potentially result in values of k_g over an order of magnitude lower than those for AR bare Crofer 22 APU.

5. Conclusions

A study was performed on the effect of 1 and 4 h pre-oxidation heat treatments at 1050 °C in Ar on the oxidation kinetics and oxide scale microstructure for Crofer 22 APU oxidized in air at 800 °C for up to 750 h. The key findings of this study were:

1. The parabolic oxidation rate constant, k_g, fell from 4.8×10^{-8} mg^2 cm^{-4} s^{-1} for the AR samples to 2.8×10^{-8} and 1.4×10^{-8} mg^2 cm^{-4} s^{-1} for the HT1h and HT4h samples, respectively.
2. All of the oxidized samples exhibited: a two-layer oxide scale with a continuous inner Cr_2O_3 layer and a discontinuous outer $MnCr_2O_4$ spinel layer, subscale $MnCr_2O_4$ spinel pockets protruding into the alloy, and internal Ti-rich oxide precipitates with the monoclinic TiO_x structure.
3. Both the grain size of the outer $MnCr_2O_4$ spinel layer and the proportion of this phase in the oxide scale increased with alloy heat treatment and increasing alloy grain size.
4. The scale microstructures for samples oxidized for just 5 h indicate that the nucleation of the Cr_2O_3 and $MnCr_2O_4$ phases during the initial stages of oxidation influences the final scale microstructures. Larger alloy grain sizes lead to lower nucleation rates, larger spinel grains, and improved oxidation resistance.

It is inferred from these observations that: the larger alloy grain sizes in the heat-treated samples reduce the initial supply of Mn to the alloy surface; this leaves more Cr available to form a thicker initial Cr_2O_3 scale with coarser grains; and the effect of this layer on the transport of Mn and Cr is what leads to the reduction in k_g. Thus, alloy heat treatment is an effective way of slowing the oxidation of Crofer 22 APU. It is suggested that a combination of alloy heat treatment and MCO coating could result in better oxidation resistance and inhibition of chromia volatility in SOFC interconnect applications than coating alone.

Acknowledgments

References

[1] H. Kurokawa, C. Jacobson, L.C. DeJonghe, S.J. Visco, Solid State Ionics 178 (2007) 287–296.
[2] M. Stanislowski, J. Froitzheim, L. Niewolak, W.J. Quadakkers, K. Hilpert, T. Markus, L. Singheiser, Journal of Power Sources 164 (2007) 578–589.
[3] C. Collins, J. Lucas, T.L. Buchanan, M. Kopczyk, A. Kayani, P.E. Gannon, M.C. Deibert, R.J. Smith, D.-S. Choi, V.I. Gorokhovsky, Surface & Coatings Technology 201 (2006) 4467–4470.
[4] J. Froitzheim, H. Ravash, E. Larsson, L.G. Johansson, J.E. Svensson, Journal of the Electrochemical Society 157 (2010) B1295–B1300.
[5] R. Trebbels, T. Markus, L. Singheiser, Journal of the Electrochemical Society 157 (2010) B490–B495.
[6] EditionCrofer 22 APU Material Data Sheet 4046, Thyssen Krupp VDM, May 2010.
[7] Z. Yang, G. Xia, G. Maupin, J. Stevenson, Journal of the Electrochemical Society 153 (2006) A1852–A1858.
[8] J. Fergus, Materials Science and Engineering A 397 (2005) 271–283.
[9] W. Liu, X. Sun, E. Stephens, M. Khaleel, Journal of Power Sources 189 (2009) 1044–1050.
[10] Z. Yang, G. Xia, X. Li, J. Stevenson, International Journal of Hydrogen Energy 32 (2007) 3648–3654.
[11] N. Magdefrau, L. Chen, E. Sun, J. Yamanis, M. Aindow, Journal of Power Sources 227 (2013) 318–326.
[12] Z. Yang, J. Hardy, M. Walker, G. Xia, S. Simner, J. Stevenson, Journal of the Electrochemical Society 151 (2004) A1825–A1831.
[13] Z. Yang, M. Walker, P. Singh, J. Stevenson, T. Norby, Journal of the Electro-chemical Society 151 (2004) B669–B678.
[14] Z. Zurek, A. Jaroń, M. Homa, Oxidation of Metals 76 (2011) 273–285.
[15] V. Trindade, U. Krupp, B. Hanjari, S. Yang, H. Christ, Materials Research 8 (4) (2005) 371–375.
[16] R. Raman, A. Khanna, R. Tiwari, J. Gnanamoorthy, Oxidation of Metals 37 (½) (1992).
[17] L. Chen, E. Sun, J. Yamanis, N.J. Magdefrau, Journal of the Electrochemical Society 157 (2010) B931–B942.
[18] D. Watanabe, J.R. Castles, A. Jostsons, A.S. Malin, Acta Crystallographica 23 (1967) 307–313.
[19] I. Saeki, H. Konno, R. Furuichi, T. Nakamura, K. Mabuchi, M. Itoh, Corrosion Science 40 (1998) 191–200.
[20] I. Saeki, H. Konno, R. Furuichi, Corrosion Science 38 (1996) 1595–1612.
[21] J. Rufner, P. Gannon, P. White, M. Deibert, S. Teintze, R. Smith, H. Chen, International Journal of Hydrogen Energy 33 (2008) 1392–1398.
[22] R.E. Lobnig, H.P. Schmidt, K. Hennesen, H.J. Grabke, Oxidation of Metals 37 (1992) 81–93.
[23] A.C.S. Sabioni, A.M. Huntz, L.C. Borges, F. Jomard, Philosophical Magazine 87 (2007) 1921–1937.
[24] M.G.C. Cox, B. McEnaney, V.D. Scott, Philosophical Magazine 31 (1975) 331–338.
[25] D. Kim, C. Jang, W.S. Ryu, Oxidation of Metals 71 (2009) 271–293.
[26] D.E. Alman, P.D. Jablonski, International Journal of Hydrogen Energy 32 (2007) 3743–3753.
[27] P. Huczkowski, N. Christiansen, V. Shemet, L. Niewolak, J. Piron-Abellan, L. Singheiser, W.J. Quadakkers, Fuel Cells 06 (2) (2006) 93–99.
[28] J. Froitzheim, G.H. Meier, L. Niewolak, P.J. Ennis, H. Hattendorf, L. Singheiser, W.J. Quadakkers, Journal of Power Sources 178 (2008) 163–173.
[29] C. Leung, M. Weinert, P.B. Allen, R.M. Wentzcovitch, Physical Review B 54 (1996) 7857–7864.
[30] M.J. Garcia-Vargas, L. Lelait, V. Kolarik, H. Fietzek, M. Juez-Lorenzo, Materials at High Temperatures 22 (2005) 245–251.
[31] J. Issartel, S. Martoia, F. Charlot, V. Parry, G. Parry, R. Estevez, Y. Wouters, Corrosion Science 59 (2012) 148–156.
[32] J.W. Fergus, Scripta Materialia 65 (2011) 73–77.
[33] K. Wang, Y. Liu, J.W. Fergus, Journal of the American Ceramic Society 94 (2011) 4490–4495.
[34] Z. Lu, J. Zhu, E.A. Payzant, M.P. Paranthaman, Journal of the American Ceramic Society 88 (2005) 1050–1053.
[35] X. Chen, P.Y. Hou, C.P. Jacobson, S.J. Visco, L.C. De Jonghe, Solid State Ionics 176 (2005) 425–433.